SRL Early Edition

Active-Source Seismic Tomography at the Brady Geothermal Field, Nevada, with Dense Nodal and Fiber-Optic Seismic Arrays

by L. M. Parker, C. H. Thurber, X. Zeng, P. Li, N. E. Lord, D. Fratta, H. F. Wang, M. C. Robertson, A. M. Thomas, M. S. Karplus, A. Nayak, and K. L. Feigl

ABSTRACT

We deployed a dense seismic array to image the shallow structure in the injection area of the Brady Hot Springs geothermal power plant in western Nevada. The array was composed of 238 three-component, 5 Hz nodal instruments, 8700 m of distributed acoustic sensing (DAS) fiber-optic cable (FOC) installed horizontally in surface trenches, and 400 m of FOC installed vertically in a borehole. The geophone array had about 60 m instrument spacing in the target zone, whereas DAS channel separations were about 1 m with an averaging (gauge) length of 10 m. The acquisition systems provided 15 days of continuous records, including active-source and ambient noise signals. A large vibroseis truck was operated at 196 locations, exciting a swept-frequency signal from 5 to 80 Hz over 20 s using three vibration modes (vertical, longitudinal, and transverse), with three sweeps per mode at each site. Sweeps were repeated up to four times at each site during four different stages of power plant operation: normal operation, shutdown, high and oscillatory injection and production, and normal operation. After removal of the sweep signal from the raw data, the first *P*-wave arrivals were automatically picked using a combination of methods. The travel times were then used to invert for the 3D *P*-wave velocity structure. Models with 100 m horizontal and 20–50 m vertical node spacing were obtained, covering an area 2000 m by 1300 m, with acceptable resolution extending to about 250 m below surface. The travel-time data were fit to a root mean square (rms) misfit of 31 ms, close to our estimated picking uncertainty. Lateral boundaries between high and low velocity zones agree relatively well with the location of local faults from previous studies, and low near-surface velocities are associated with faults and fumarole locations. A sharp increase in velocity from < 1500 to > 2000 m/s at approximately 50 m below the ground surface in many parts of the study area may indicate a shallower water table than expected for the region.

INTRODUCTION

The Poroelastic Tomography by Adjoint Inverse Modeling of Data from Seismology, Geodesy, and Hydrology (PoroTomo) project is an integrated, multidisciplinary assessment of methods for shallow geothermal reservoir characterization and monitoring. The natural laboratory of the Brady Hot Springs geothermal power plant was chosen as the site for the PoroTomo project, in part due to the presence of multiple shallow subsidence signatures shown in satellite interferometric synthetic aperture radar (Ali *et al.*, 2016). The project's goal is to assess an integrated technology for characterizing the physical properties of a shallow volume of the area where the subsidence is occurring, using multiple geophysical methods (Feigl and PoroTomo Team, 2017, 2018). In this article, we report results from *P*-wave first arrivals seismic tomography using vibroseis sources recorded on a combined array of distributed acoustic sensing (DAS) and 238 three-component, 5-Hz FairfieldNodal seismic nodes. We compare the resulting velocity models with regional geologic maps and hydrologic data.

GEOLOGIC BACKGROUND

Several bands of geothermal fields stretch across the northwestern Great Basin in the United States (Fig. 1). The Humboldt Structural Zone is one such feature and includes several high-temperature geothermal systems with temperatures in excess of 160°C (Faulds *et al.*, 2004). Volcanism in the region ceased between 10 and 3 Ma (Faulds *et al.*, 2006), and many of the geothermal systems are considered to have amagmatic heat sources (Faulds *et al.*, 2004). North-northeast-striking faults orthogonal to the direction of the regional extension are considered to be the primary control on the location and structure of the geothermal systems (e.g., Faulds *et al.*, 2004, 2006; Faulds, Moeck, *et al.*, 2010).

Most of the geothermal systems in this region are found in areas with steeply dipping (> ~50°) normal fault zones rather than range-front faults (Faulds *et al.*, 2006). At these normal fault zones, fractures appear to facilitate deep circulation of thermal waters (Faulds *et al.*, 2004, 2006). In particular, local structural features in the fault system such as step-overs and jogs are the common sites of geothermal systems (Faulds *et al.*, 2004). Faulds *et al.* (2003) suggest that a small component of

doi: 10.1785/0220180085

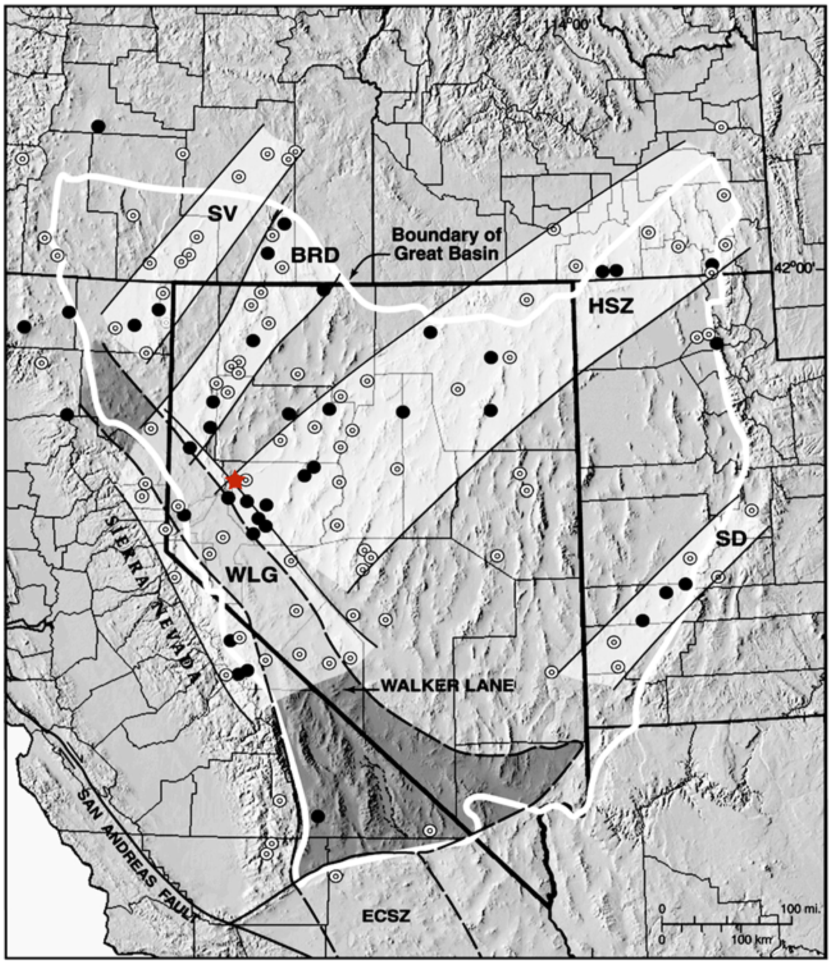

▲ **Figure 1.** Map of geothermal fields in the Great Basin, modified from Faulds *et al.* (2004). Geothermal field belts are the Sevier Desert (SD), Humboldt Structural Zone (HSZ), Black Rock Desert (BRD), Surprise Valley (SV), and Walker Lane Geothermal (WLG). Circles are geothermal systems; white for maximum temperatures below 160°C and black for maximum temperature above 160°C. Star marks Brady Hot Springs geothermal field. ECSZ, eastern California shear zone. The color version of this figure is available only in the electronic edition.

sinistral shear associated with many en echelon overlapping normal faults combined with the regional extension leads to locally greater fault and fracture density. Permeable stratigraphic units are also important for localizing geothermal reservoirs and facilitating fluid transmissivity (Faulds *et al.*, 2003).

Brady geothermal field is located in the Hot Springs Mountains. The geology of the region consists of Mesozoic plutonic–metamorphic basement overlain by late Oligocene to late Miocene volcanic and sedimentary rocks (Faulds and Garside, 2003; Faulds, Coolbaugh, *et al.*, 2010; Faulds, Moeck, *et al.*, 2010; Faulds *et al.*, 2012; see Fig. 2). The Hot Springs Flat basin that lies to the west of the Hot Springs Mountains consists of late Miocene to Quaternary basin-fill sediments with the Quaternary sediments dominated by lacustrine deposits (Faulds and Garside, 2003; Faulds, Coolbaugh, *et al.*, 2010; Faulds, Moeck, *et al.*, 2010; Faulds *et al.*, 2012). The region is broken into multiple north-northeast-trending blocks by north-northeast-striking normal faults (Fig. 2). Multiple dating methods indicate that the major episode of extension occurred from 13 to 9 Ma (Faulds *et al.*, 2006; Faulds, Coolbaugh, *et al.*, 2010).

The Brady fault zone forms the northwestern boundary of the Hot Springs Mountains and is the main structural control in the Brady geothermal field (Faulds, Moeck, *et al.*, 2010). It dips 60°–80° to the northwest (Jolie *et al.*, 2015), with the main fault accommodating ~150 m of throw (Benoit *et al.*, 1982; Faulds *et al.*, 2003). The surface expression of the geothermal field extends 4 km along the Brady fault zone as fumaroles, warm ground, sinter deposits, and mud pots (Faulds, Coolbaugh, *et al.*, 2010; Faulds, Moeck, *et al.*, 2010; Jolie *et al.*, 2015). A geologic map of the Brady study is shown in Figure 2, and the locations of surface geothermal features and major faults are shown in Figure 3a.

DATA AND METHODS

The PoroTomo Project deployed several sets of instruments at the Brady Geothermal power plant in March 2016 (Feigl and PoroTomo Team, 2017, 2018). In conjunction with that deployment, the operation of the power plant was intentionally varied to produce four different time intervals of injection and production activity, constituting the four stages of this experiment. The first stage was characterized by normal rates of injection and extraction by the power plant, the second stage was characterized by limited fluid extraction from or injection into the reservoir (the plant was shut down for maintenance), the third stage was characterized by high and variable rates of injection and extraction, and the fourth stage was characterized by a return to normal injection and extraction rates.

The seismic instrumentation used for our tomographic modeling consisted of a nodal array and a DAS system. The nodal seismic array, consisting of 238 three-component, 5-Hz FairfieldNodal Z-L and 3C instruments, was deployed over an ~2000 m by 1300 m area. In the central 1500 m by 500 m part of the array, these instruments were spaced approximately 60 m apart, with the outer portions of the array having approximately 200 m spacing (Fig. 3b). For the DAS system, 8700 m of 6.1 mm abrasion- and rodent-resistant fiber optic cable with acrylate-coated fibers rated to 85°C was deployed in backfilled trenches at a depth of ~0.5 m throughout the field area (Fig. 3b). DAS is a recently developed technology that has been used primarily for vertical seismic profiling in oil and gas reservoirs (Mestayer *et al.*, 2011; Mateeva *et al.*, 2014), but has also been

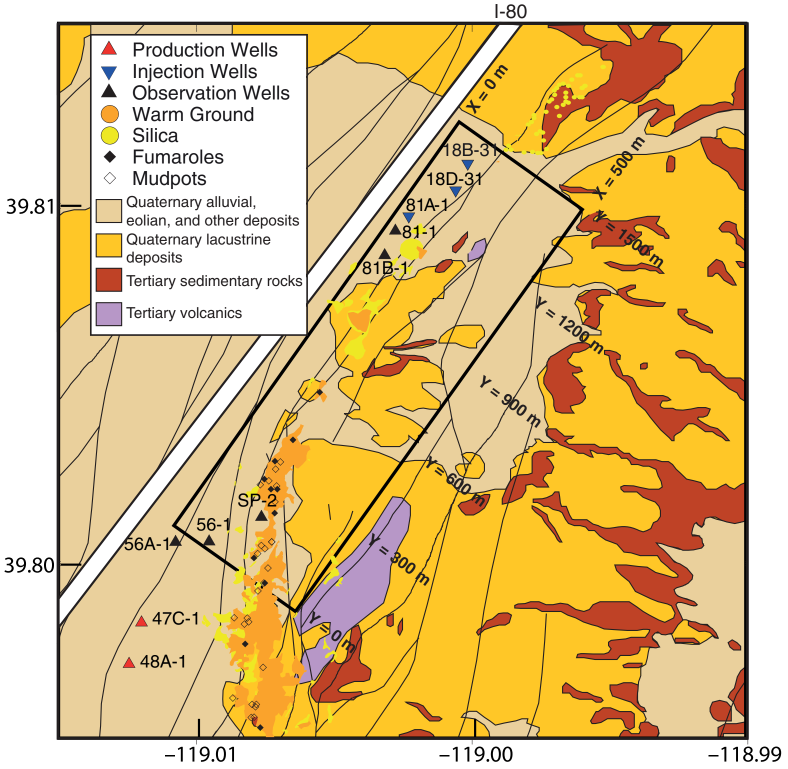

▲ **Figure 2.** Simplified geologic map of the Brady geothermal field modified from Faulds *et al.* (2017). The black rectangle corresponds to the target region where the seismic nodes were closely spaced. The surface geothermal features mapped by Coolbaugh *et al.* (2004) have been overlaid approximately. The white strip denotes the approximate location of Interstate highway 80. The color version of this figure is available only in the electronic edition.

used in small-scale surface or near-surface deployments (Daley *et al.*, 2013; Lancelle, 2016; Zeng *et al.*, 2017; Castongia *et al.*, 2017; Dou *et al.*, 2017; Wang *et al.*, 2018). A DAS interrogator system sends a very short laser pulse into the fiber at a high repeat rate, and the interrogator records the returning arrivals from Rayleigh scattering off imperfections within the cable. Seismic waves deform the cable, affecting the two-way travel time of the returned laser pulses. Consecutive pulses are then captured to estimate the strain rate of the seismic waves on the DAS cable. Laser pulses were recorded and interpreted with a Silixa interrogator system. The interrogator recorded return arrivals from approximately every meter along the cable, with a spatial averaging length of 10 m. Some 370 m of 3.2 mm fiber in metal tube cable with carbon-polyimide-coated fibers rated to 150°C was also deployed down an observation well (Fig. 3b) to provide sampling to greater depths. However, because of deployment delays, the downhole cable was only installed in time to record stages 3 and 4 and no infill was available to increase coupling to the wellbore casing (and thus the rock formation). Usable borehole DAS data were limited to depths greater than ~160 m below surface ($Z \sim 1090$ m), where we infer that the casing is adequately cemented to the surrounding rock. The nodal and horizontal DAS arrays provided 15 days

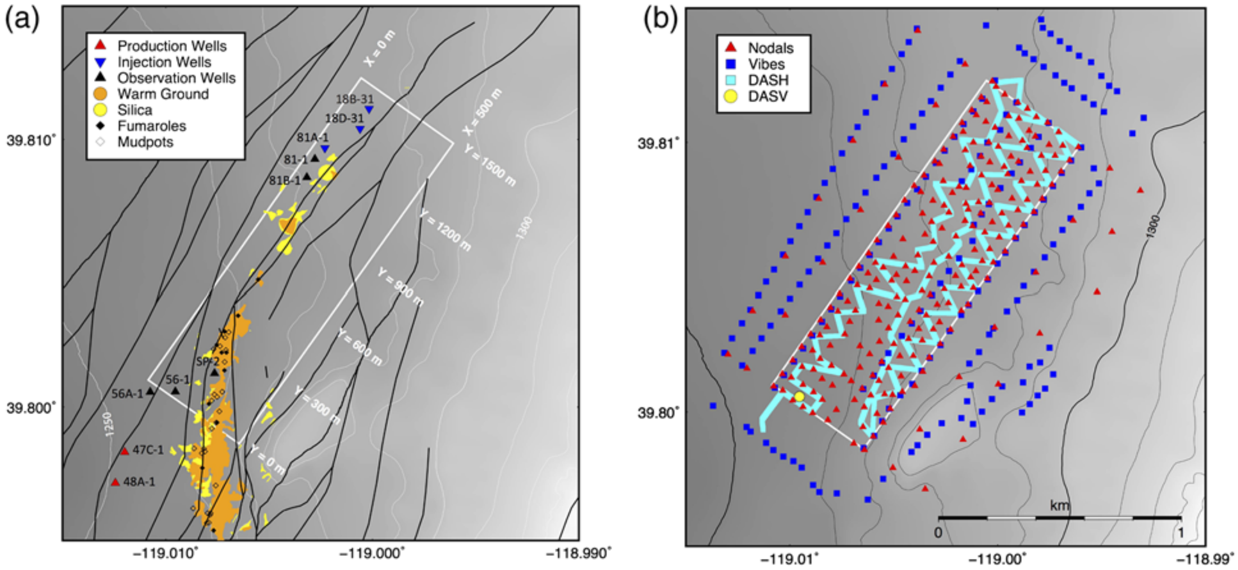

▲ **Figure 3.** (a) Map of geothermal surface features at Brady Hot Springs geothermal field, from Coolbaugh *et al.* (2004), with 10 m elevation contour intervals. Elevations are meters above the WGS84 ellipsoid. The box corresponds to the target region, the densest part of the nodal seismometer array. (b) Map of instrument array and vibrator locations, with 10 m elevation contour intervals. Elevations are meters above the WGS84 ellipsoid. The white box corresponds to the target region, the densest part of the nodal seismometer array. DASH is the horizontally deployed distributed acoustic sensing (DAS) cable (wide line segments) and DASV is the location of the vertically deployed DAS cable, that is, in a borehole (circle). The color version of this figure is available only in the electronic edition.

of continuous records. The vertical DAS array provided 7 days of continuous records.

A large vibroseis truck, a 285 kN high-force tri-axial shaker known as "T-Rex" and owned and operated by the University of Texas at Austin, was used to generate the active-source seismic signals (Stokoe *et al.*, 2004). It was operated at 196 locations (Fig. 3b), occupying each location up to four times over the course of 15 days, once for each stage. It excited a swept-frequency signal from 5 to 80 Hz over 20 s using three vibration modes, vertical, longitudinal, and transverse, for a total of 6633 vibroseis events. Only results from the vertical vibration mode are presented as it produced the strongest *P*-wave signals.

Survey-grade Global Positioning System equipment was used to survey each of the nodal seismometer locations, the locations of DAS fiber-optic cable channels (those channels identified by a tap test), and the vibroseis source locations. Source and node orientations were measured with compasses. Positions are accurate to 5 cm and source orientations to 1°.

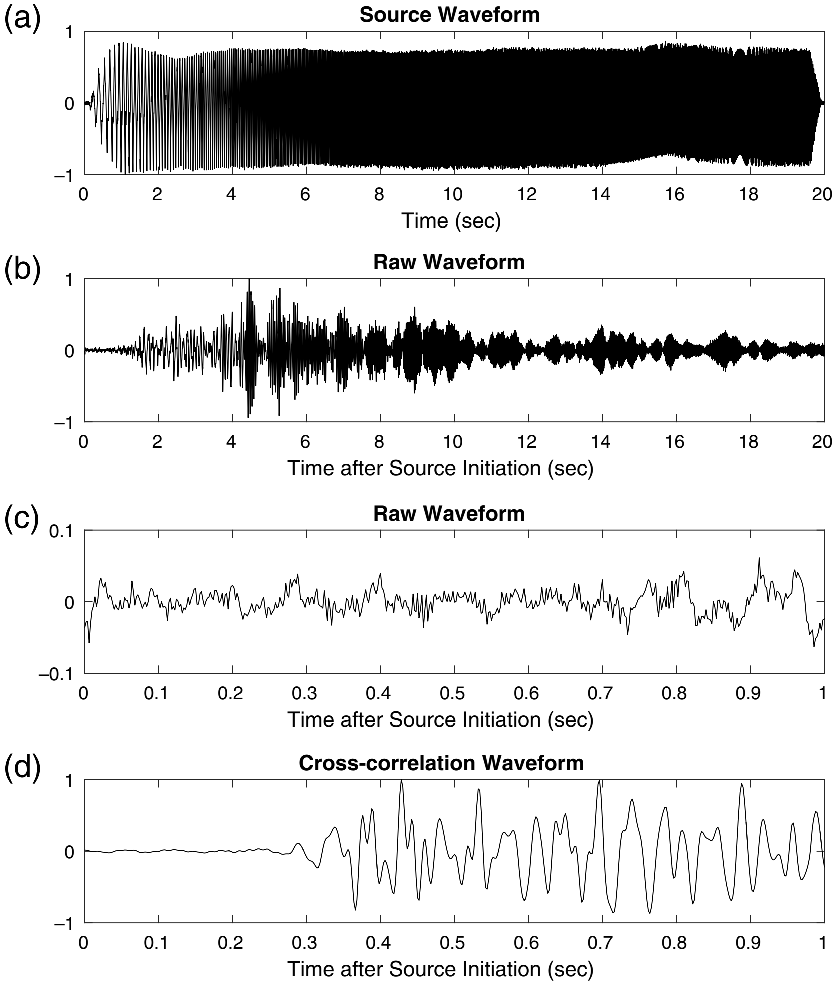

▲ **Figure 4.** (a) Example of a source sweep recorded at the vibroseis truck. (b) Example of the raw data for the same sweep recorded at a nodal seismometer located 440 m away. (c) The same raw waveform zoomed in to the time of the initial sweep signal arrival. (d) Cross-correlation results zoomed in to show the first arrival.

Data Processing

Although swept-frequency sources have the advantage of repeatability, the nonimpulsive nature of a swept-frequency source makes it difficult to determine the first arrival of seismic waves (Fig. 4b). In order to see the equivalent of a first arrival, one must first remove the swept-frequency signal from the waveforms. To this end, several different methods have been developed (Brittle *et al.*, 2001; Ikuta *et al.*, 2002; Saiga *et al.*, 2006; Li *et al.*, 2013). The two most common methods are source signal cross correlation and deconvolution (Brittle, 2001). We used a linear combination of seismic data from accelerometers located on the reaction mass and the base plate of T-Rex for each vibe record as the source signal (Fig. 4a), except for a small number of cases when that record was unavailable. In those cases, the theoretical ("pilot") sweep was used instead. A comparison of the two methods of source signal removal on example data from Brady showed that their results were very similar, but a slightly higher signal-to-noise ratio (SNR) was obtained with the cross-correlation method, so it was chosen for removing the sweep signal. An example is shown in Figure 4c,d. The next step was to stack the cross-correlation waveforms to further improve the SNR. Stacks involved all instances of a sweep mode at a vibe point for each stage of the experiment. Stacking was carried out after cross correlation, as the source waveform was unique for each sweep.

In order to process the large volume of waveforms and to maximize the number of picks, it was necessary to use an automatic phase arrival picker. There is no standard method for picking first *P*-wave arrivals from vibroseis data, so we tested several autopickers using a spatially representative subset of the data during stage 2 when the background noise was lowest. The autopickers with the best results were an Akaike information criterion (AIC) algorithm (Sleeman and Van Eck, 1999; Akram and Eaton, 2016) and a short- and long-term average ratio (STA/LTA) algorithm (Trnkoczy, 2009; Akram and Eaton, 2016).

Based on success in comparison to analyst picks and more consistent distance versus time trends, we initially chose to use the AIC autopicker. To improve the quality of the picks, we ran a 3D tomographic inversion using the picks from this data subset that fell within the predominant travel-time trend with distance. From the resulting model, we generated a set of predicted travel times from all vibe points to all receivers. Subsequent runs of the autopicker picked the best arrival within 0.1 s before and 0.2 s after the predicted travel time for each receiver–source pair (Fig. 5a). These new bounds were able to account for variations in travel time (late arrivals were more likely than early arrivals) while reducing the size of the picking window on average.

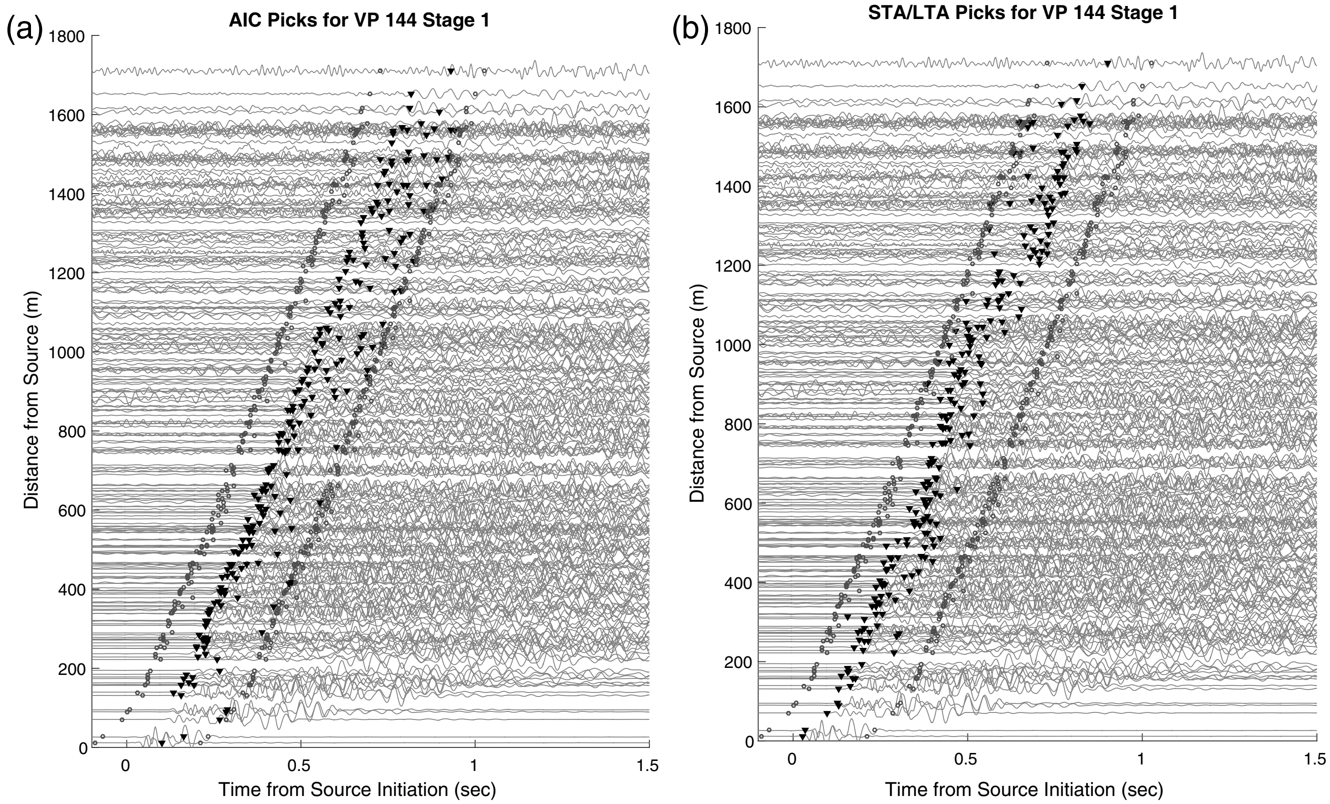

▲ **Figure 5.** (a) Pick times from the Akaike information criterion (AIC) autopicker overlain on the stacked cross-correlation waveforms plotted by distance from the source. Inverted triangles mark the pick times and circles mark the bounds for making picks. (b) Pick times from the short-term average/long-term average ratio (STA/LTA) autopicker overlain on the stacked cross-correlation waveforms plotted by distance from the source. Inverted triangles mark the pick times and circles mark the bounds for making picks.

After applying the AIC autopicker to more data, we observed that it typically failed to correctly pick the *P*-wave arrival for waveforms from stations within 150 m of the source. It often picked the secondary air-wave arrival instead of the *P*-wave arrival due to the greater energy of the air wave at those distances. To obtain these near-distance arrivals, we elected to use the STA/LTA autopicker when the recorder was within 150 m of the source (Fig. 5b). The total number of picks was 44,268 for stage 1, 38,719 for stage 2, 41,520 for stage 3, and 42,518 for stage 4.

To weight the travel-time picks from the nodal data for the tomographic inversion, SNR was measured for each pick. These SNR values were calculated by dividing the root mean square (rms) amplitude of a window 0.2 s after the pick time by the rms amplitude of a window 0.2 s before the pick. The noise window was chosen to be directly before the pick rather than at a fixed time with no signal because it was desirable to penalize picks of the air-wave arrival rather than the *P*-wave arrival. Because of the strength of the air-wave arrival in some of our waveforms from the nodal seismometers, a standard SNR noise window would have a good SNR value for an air-wave arrival, whereas using a noise window directly before the air-wave pick would include the energy from the *P*-wave arrival and reduce the SNR.

The same AIC autopicker was applied to the vertical DAS (DASV) and horizontal DAS (DASH) records. Channels every 10 m were used from the DASH array. Channels from 166 to 346 m along the length of the DASV cable were used because this was the segment of the cable that was sufficiently coupled with the well to yield clear signals. Channels every 5 m were used to balance the number of receiver locations at depth against the amount of overlap in signals due to the 10 m gauge length. The SNR of the vibe source was only high enough to pick arrivals for the 17 nearest vibe locations for DASV, yielding 305 picks for stage 3 and 323 for stage 4. For DASH, 45,989 arrivals were picked for stage 4. SNR ratios for each point were measured using a set noise window because the air-wave did not complicate the *P*-wave arrival in the DAS data.

In Figure 6, we show examples of representative picks on DAS channels compared with picks on nearby nodes. The figure illustrates both the differences in the character of the two data types and the difficulty of making high-quality picks. Recall that the DAS system yields records of strain rate, whereas the nodal instruments provide velocity records. Note also that the nodal records are from the vertical channel, which was used for autopicking, but the DAS records are of horizontal strain rate. Thus, the data shown compare the records that were used for picking rather than represent an apples-to-apples compari-

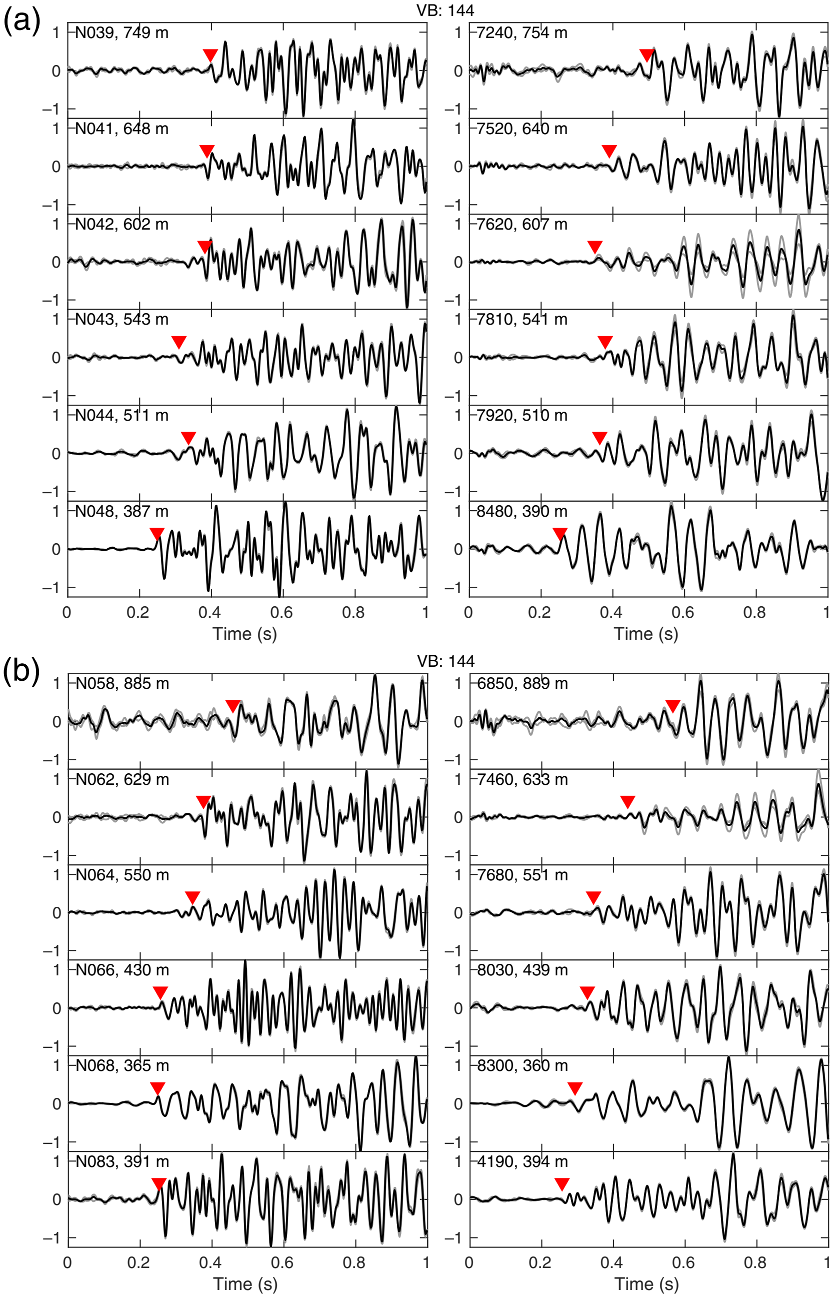

▲ **Figure 6.** (a,b) Comparison of nodal data (left panels, with node number and distance from the vibe point indicated) with DAS data (right panels, with DAS channel number and distance from the vibe point indicated) and the associated autopicks (inverted triangles) for a vibe point near the north corner of the target area. The gray lines (which generally are difficult to see) are from individual sweeps and the black line is the stack. The color version of this figure is available only in the electronic edition.

son of the waveforms. See Wang *et al.* (2018) for a detailed comparison of the two data types for equalized records of a regional earthquake—that is, nodal data transformed to strain rate and DAS data transformed to particle velocity. Here, we note that the nodal records typically have more high-frequency content and a higher signal-to-noise ratio. The former can be attributed at least in part to the intrinsic difference between velocity records, which are a temporal derivative of particle displacement at a point, and strain-rate records, which are a temporal derivative of spatial strain averaged over the gauge length.

Tomographic Inversion

To obtain a 3D V_P model, we used the simul2000 tomography code (Thurber and Eberhart-Phillips, 1999). Source and receiver locations were transformed into a Cartesian coordinate system centered on the southwest corner of the inner portion of the nodal seismometer array at 39.8010° N and 119.0108° W, with the Y axis oriented at about 36° azimuth to be parallel to the average north-northeast strike of the normal faults and the long axis of the study area (Fig. 3). Sources and receivers were modeled at their true elevations. The inversion grid for the final model is 2000 m long in the X direction and 1300 m wide in the Y direction, with horizontal spacing of the grid nodes of 100 m except for the outside edges where the spacing is 200 m. Grid nodes in the Z direction were positioned at 1250 m (close to the surface), 1230, 1210, 1190, 1150, 1100, 1050, 1000, 900, 800, and 600 m, with 0 m corresponding to the World Geodetic System 1984 (WGS84) ellipsoid.

The simul2000 code (Thurber and Eberhart-Phillips, 1999) uses the pseudobending method of Um and Thurber (1987) for raytracing and employs a damped least-squares inversion. A damping parameter governs the trade-off between data misfit and model perturbations. The code also provides complete information on model resolution and uncertainty. We constructed a trade-off curve to compare the model results for final misfit versus total model perturbation (variance) for damping values of 0.02, 0.1, 0.5, 2, 8, and 40. The "knee" of the trade-off curve was found at a damping value of 2. Based on the diagonal elements of the model resolution matrix (Aster *et al.*, 2012) that are computed by the simul2000 algorithm, we find that model resolution is reasonably good above ~1000 m elevation (~250 m below surface) in the 1500 m by 500 m target area. A checkerboard test with 100 m size anomalies supports this result (Fig. 7). The velocity anomalies were recovered within 1% for nearly 70% of the grid nodes. We note that tomographic inversions, including the DAS data, provided substantially improved model resolution compared with ones without the DAS data, although the resulting velocity model values themselves were not very different (typically within 1%–2%).

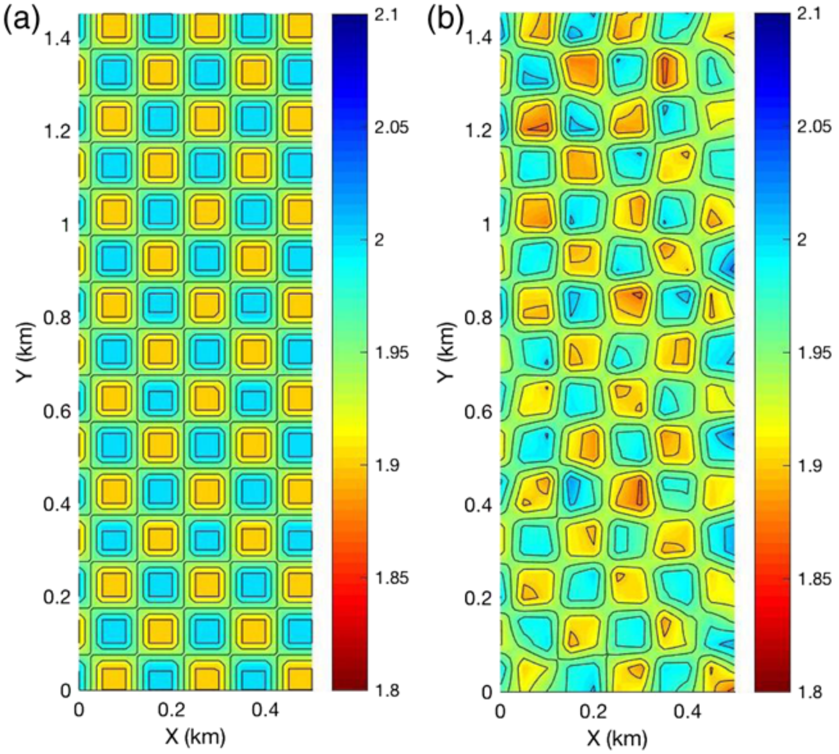

▲ **Figure 7.** Checkerboard test results at 150 m depth. (a) Input anomalies and (b) recovered anomalies. The color version of this figure is available only in the electronic edition.

RESULTS AND DISCUSSION

Figure 8 shows horizontal slices and Figure 9 shows northwest-to-southeast-oriented cross sections of the V_P model for the tomographic inversion using P-wave picks from the nodal seismometers, DASH, and DASV. In the near-surface slices, low-velocity zones dominate the model. These velocities are consistent with the expected values of the alluvial deposits found near the surface (Fig. 2; Queen *et al.*, 2016). Based on well-log lithologies (Figs. 3a and 10), the alluvial deposits extend to greater depths in the northern part of the study area compared with the southern part. In the southern well, 56A-1 (Fig. 10f), an alluvium thickness of ~50 m (Z ~1200 m) is consistent in depth with a transition from slower (< 1500 m/s) to faster (> 2000 m/s) velocities, a transition that is present in much of the southern part of the model (Figs. 8 and 9). The seismic velocity of water-saturated sediments generally exceeds the speed of sound in water (about 1480 m/s) but is dependent on porosity, water saturation, and lithology (e.g., Mavko *et al.*, 2009). In the northern well logs, the Quaternary alluvial deposits extend to greater depths, and the depth

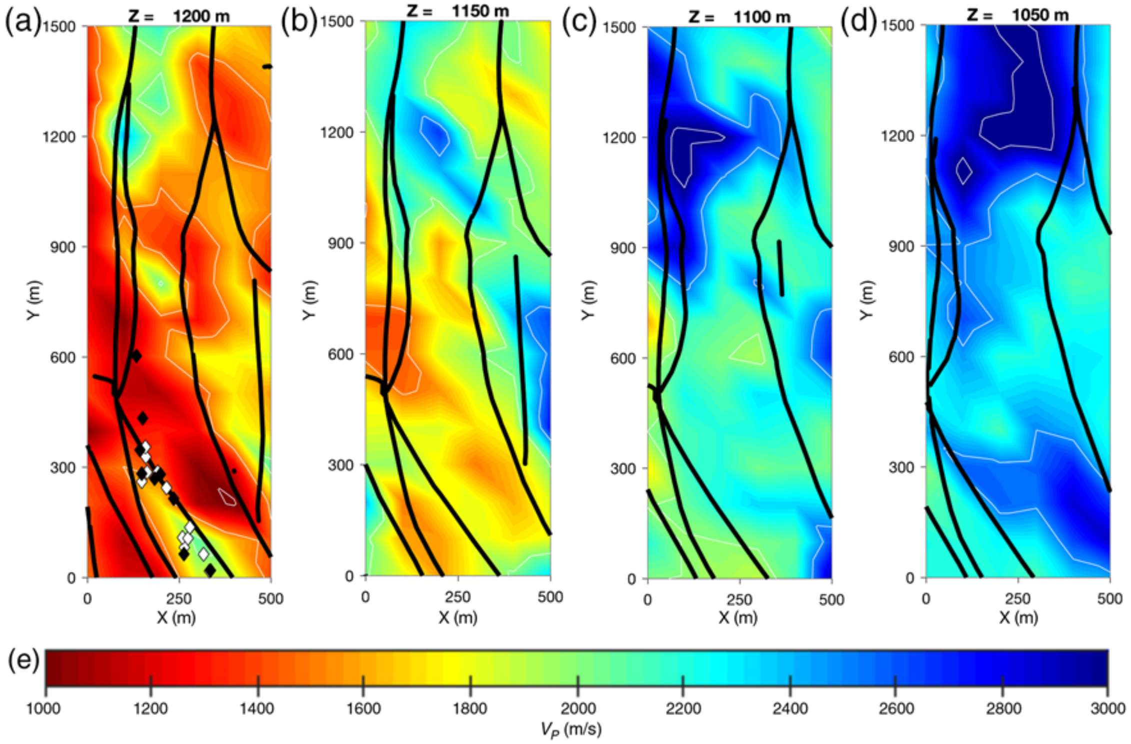

▲ **Figure 8.** Representative depth slices through the 3D V_P model, at elevations Z with respect to the World Geodetic System 1984 (WGS84) ellipsoid of (a) 1200 m, (b) 1150 m, (c) 1100 m, and (d) 1050 m. Contours are at 1000 m/s intervals. Thick lines are intersections of faults (from Siler *et al.*, 2016) with each depth slice. The rectangle is the target region, as shown in Figures 3a,b. Black and white diamonds in (a) are fumaroles and mudpots, respectively. (e) V_P color scale. The color version of this figure is available only in the electronic edition.

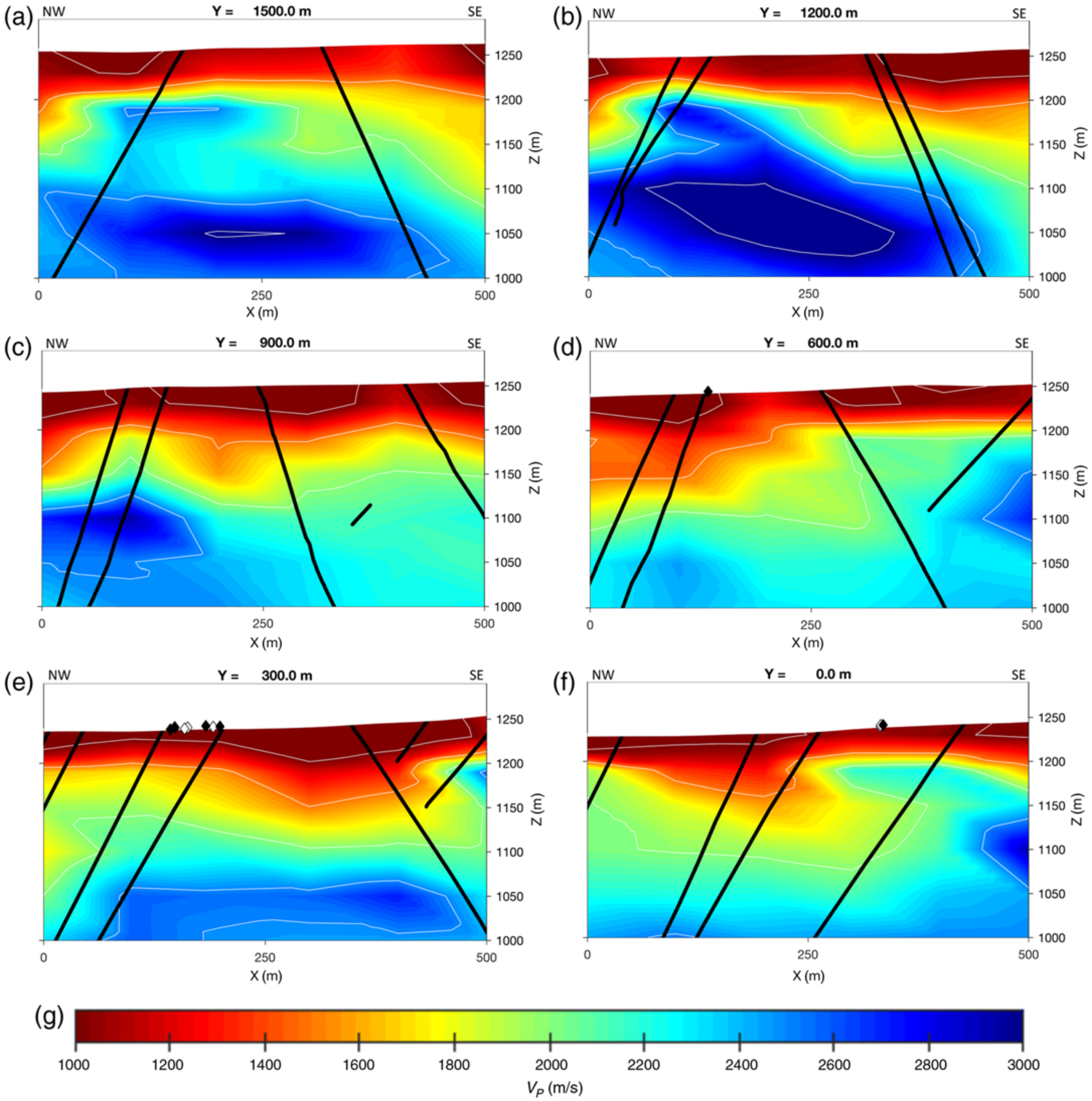

▲ **Figure 9.** Representative northwest to southeast cross sections through the 3D V_P model, at Y coordinates of (a) 1500 m (northeast edge of the target region), (b) 1200 m, (c) 900 m, (d) 600 m, (e) 300 m, and (f) 0 m (southwest edge of the target region). Contours are at 1000 m/s intervals. Elevations, Z, are with respect to the WGS84 ellipsoid. Thick lines are intersections of faults (from Siler *et al.*, 2016) with each cross section. Fault dips are generally ~50°–60°. Black and white diamonds are fumaroles and mudpots, respectively. (g) V_P legend. The color version of this figure is available only in the electronic edition.

of this velocity transition zone is fairly uniform, but transition depth in the velocity model does not occur at the same depth as boundaries in the logs (Fig. 10). This may be due to the presence of the water table or perched water just above the Tertiary deposits, which could imply the presence of water at a shallower depth than the reported regional value of ~100 m (Patterson *et al.*, 2017). Alternately, the velocity changes could be related to changes in water saturation, porosity, or other factors.

In the rest of the study area, the faster velocities (~2400–3000 m/s) at greater depths (elevation < ~1100 m)

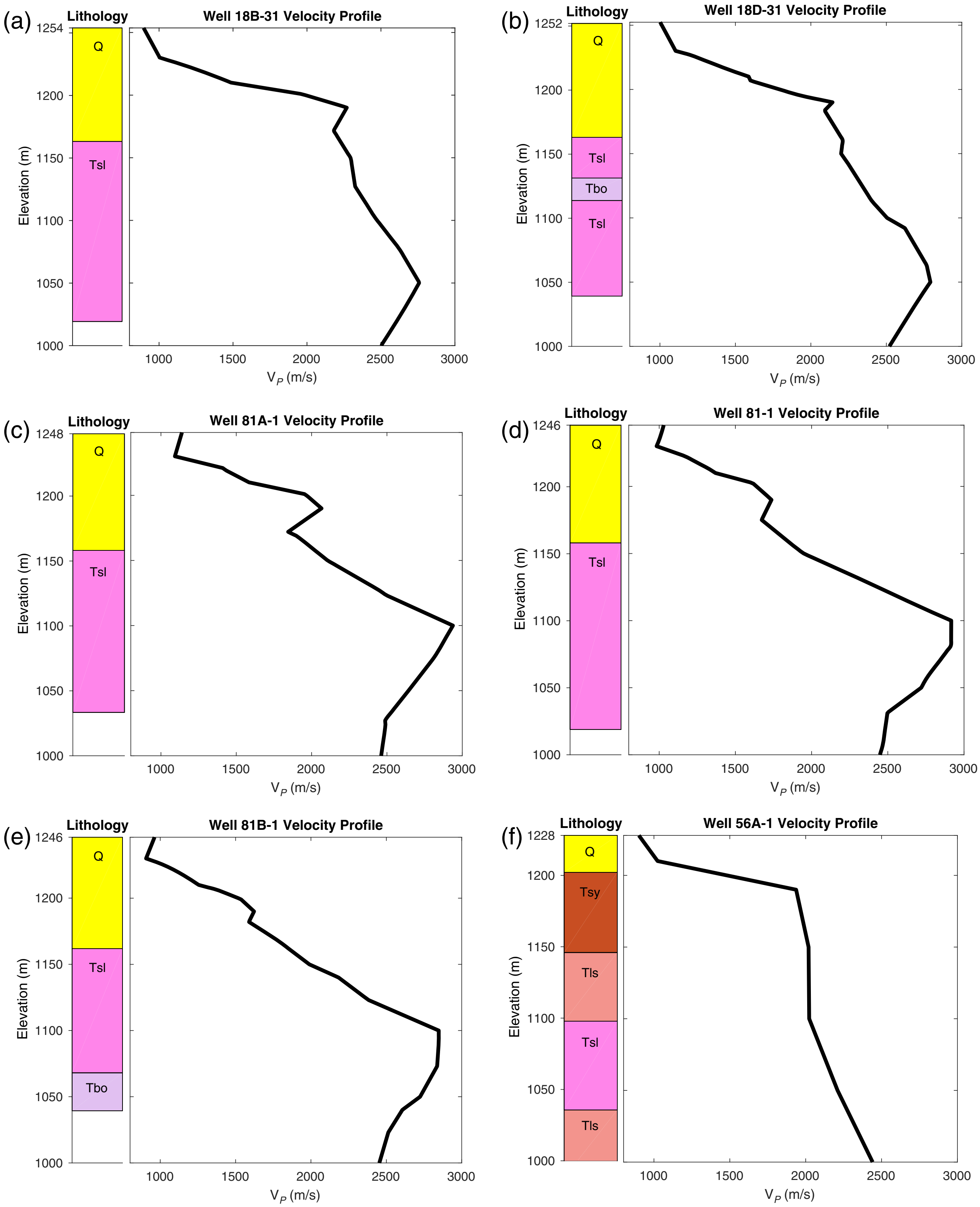

▲ **Figure 10.** Comparisons of lithology from well logs (Siler *et al.*, 2016) and V_P from each well's location in the 3D V_P model. See Figure 3a for location of the wells. Q, Quaternary sediments; Tsl, lacustrine sediments; Tbo, Tertiary basalts; Tls, limestone; Tsy, sandstone and conglomerate. The color version of this figure is available only in the electronic edition.

fall within the reported seismic velocities for tuff (Wohletz and Heiken, 1992) and sedimentary deposits (Bourbié and Coussy, 1987). We interpret the abrupt lateral changes in velocity visible in the cross sections (Fig. 9) as faults juxtaposing rocks with different seismic velocities. In particular, the high V_P at depth in the $Y = 300$ m cross section in the central part of the model (Fig. 9e) is approximately bounded by faults with much lower velocities on either side. Similar structures can also be seen in the $Y = 1200$ and 1500 m cross sections at depth on the southeast side of the model (Fig. 9a,b). The other main feature that is apparent at shallow depths, particularly in the $Z = 1200$ m slice (Fig. 8a, ~50 m below the surface), is the zone of low velocities that strikes northeast, roughly parallel to and along the northwest edge of the long (Y) axis of the study area. The low velocities extend to greater depth (Fig. 8b) and are closely aligned with the trend of the major faults and the trend of fumaroles and mudpots (Figs. 8b, 9e).

CONCLUSIONS

We performed *P*-wave velocity tomography for the Brady Hot Springs geothermal field using active-source data from a combined array of DAS and nodal seismometers. Cross correlation proved to be better than deconvolution for removing the vibroseis sweep signal from the recorded waveforms for this dataset. Autopickers were successful at picking the *P*-wave arrival for both types of data, although the downhole DAS had a very limited range of distance to the vibe locations for which the arrivals were discernable. In general, the nodal data showed higher signal-to-noise ratios and more high-frequency content than the DAS data, as expected because the DAS data are 10 m averages of strain rate, whereas the nodal data are point measurements of ground velocity. The *P*-wave velocity model showed clear velocity contrasts across a number of faults inferred by previous studies (Jolie, 2014; Jolie *et al.*, 2015; Siler *et al.*, 2016). Low-velocity zones near the surface are found close to fumarole locations, and there is a marked increase in velocity near the bottom of the injection wells. Comparisons with available well logs show a reasonable correspondence between velocity and lithology, but suggest a somewhat shallower water table than a regional estimate. Future work will include an effort to increase the number and improve the quality of the picks using more sophisticated methods.

DATA AND RESOURCES

The data used herein are available on the Geothermal Data Repository at http://gdr.openei.org/, keyword: PoroTomo.

ACKNOWLEDGEMENTS

The Geothermal Technologies Office of the U.S. Department of Energy supported this research through Grant DE-EE0006760. John Akerley, Janice Lopeman, and Paul Spielman of ORMAT Technologies generously provided access to the site and cooperated with the entire PoroTomo project. The authors thank Fan-Chi Lin for loaning nodal instruments, Jamie Farrell for assistance with the nodal data, and Incorporated Research Institutions for Seismology–Program for the Array Seismic Studies of the Continental Lithosphere (IRIS-PASSCAL) for loaning RefTek dataloggers and sensors. The facilities of the Incorporated Research Institutions for Seismology (IRIS) Consortium are supported by the National Science Foundation under Cooperative Agreement EAR-1261681 and the Department of Energy (DOE) National Nuclear Security Administration.

REFERENCES

Akram, J., and D. W. Eaton (2016). A review and appraisal of arrival-time picking methods for downhole microseismic data, *Geophysics* **81,** KS67–KS87.

Ali, S. T., J. Akerley, E. C. Baluyut, M. Cardiff, N. C. Davatzes, K. L. Feigl, W. Foxall, D. Fratta, R. J. Mellors, P. Spielman, H. F. Wang, and E. Zemach (2016). Time-series analysis of surface deformation at Brady Hot Springs geothermal field (Nevada) using Interferometric Synthetic Aperture Radar, *Geothermics* **61,** 114–120, doi: 10.1016/j.geothermics.2016.01.008.

Aster, R., B. Borchers, and C. Thurber (2012). *Parameter Estimation and Inverse Problems*, Second Edition, Elsevier, Waltham, Massachusetts, 360 pp.

Benoit, W., J. Hiner, and R. Forest (1982). Discovery and geology of the Desert Peak geothermal field: A case history, *Nevada Bureau of Mines and Geology Bulletin 97*, 82 pp.

Bourbié, T., and O. Coussy (1987). *Acoustics of Porous Media*. Éd. Technip, Paris, London.

Brittle, K. F. (2001). Vibroseis deconvolution: Frequency-domain methods, *M.S. Thesis*, University of Calgary, Alberta, 174 pp.

Brittle, K. F., L. R. Lines, and A. K. Dey (2001). Vibroseis deconvolution: A comparison of cross-correlation and frequency-domain sweep deconvolution, *Geophys. Prospect.* **49,** 675–686.

Castongia, E., H. F. Wang, N. Lord, D. Fratta, M. Mondanos, and A. Chalari (2017). An experimental investigation of distributed acoustic sensing (DAS) on lake ice, *J. Environ. Eng. Geophys.* **22,** 167–176.

Coolbaugh, M. F., C. Sladek, C. Kratt, and G. Edmondo (2004). Digital mapping of structurally controlled geothermal features with GPS units and pocket computers, *Geotherm. Resour. Counc. Trans.* **28,** 321–325.

Daley, T., B. M. Freifeld, J. Ajo-Franklin, S. Dou, R. Pevzner, V. Shulakova, S. Kashikar, D. E. Miller, J. Goetz, J. Henninges *et al.* (2013). Field testing of fiber-optic distributed acoustic sensing (DAS) for subsurface seismic monitoring, *The Leading Edge* **32,** 699–706, doi: 10.1190/tle32060699.1.

Dou, S., N. Lindsey, A. M. Wagner, T.M. Daley, B. Freifeld, M. Robertson, J. Peterson, C. Ulrich, E. R. Martin, and J. B. Ajo-Franklin (2017). Distributed acoustic sensing for seismic monitoring of the near surface: A traffic-noise interferometry case study, *Scientif. Rept.* **7,** 11620, 12, doi: 10.1038/s41598-017-11986-4.

Faulds, J. E., and L. J. Garside (2003). Preliminary geologic map of the Desert Peak—Brady geothermal fields, Churchill County, Nevada, *Nevada Bureau of Mines and Geology, Open-File Rept. 03–27*.

Faulds, J. E., M. F. Coolbaugh, D. Benoit, G. L. Oppliger, M. Perkins, I. Moeck, and P. Drakos (2010). Structural controls of geothermal activity in the Northern Hot Springs Mountains, Western Nevada: The tale of three geothermal systems (Brady's, Desert Peak, and Desert Queen), *Geotherm. Resour. Counc. Trans.* **34,** 675–683.

Faulds, J. E., M. Coolbaugh, G. Blewitt, and C. D. Henry (2004). Why is Nevada in hot water? Structural controls and tectonic model of geothermal systems in the northwestern Great Basin, *Geotherm. Resour. Counc. Trans.* **28,** 649–654.

Faulds, J. E., M. F. Coolbaugh, G. S. Vice, and M. L. Edwards (2006). Characterizing structural controls of geothermal fields in the northwestern Great Basin: A progress report, *Geotherm. Resour. Counc. Trans.* **30,** 69–76.

Faulds, J. E., L. J. Garside, and G. L. Oppliger (2003). Structural analysis of the Desert Peak-Brady geothermal field, Northwestern Nevada: Implications for understanding linkages between northeast-trending structures and geothermal reservoirs in the Humboldt structural zone, *Geotherm. Resour. Counc. Trans.* **27,** 859–864.

Faulds, J. E., I. Moeck, P. Drakos, and E. Zemach (2010). Structural assessment and 3D geological modeling of the Brady's geothermal area, Churchill county (Nevada, USA): A preliminary report, *Proc.: 35th Workshop on Geothermal Reservoir Engineering, Stanford University, Stanford, California*, SGP-TR-188, 298–302.

Faulds, J. E., A. R. Ramelli, M. F. Coolbaugh, N. H. Hinz, L. J. Garside, and J. H. Queen (2017). Preliminary geologic map of the Bradys geothermal area, Churchill County, Nevada, *Nevada Bureau of Mines and Geology, Open-File Rept. 2017–04.*

Faulds, J. E., A. R. Ramelli, L. J. Garside, M. F. Coolbaugh, and H. L. Green (2012). Preliminary geologic map of the Desert Peak quadrangle, Churchill County, Nevada, *Nevada Bureau of Mines and Geology, Open-File Rept. 12-5.*

Feigl, K. L., and PoroTomo Team (2017). Overview and preliminary results from the PoroTomo project at Brady Hot Springs, Nevada: Poroelastic tomography by adjoint inverse modeling of data from seismology, geodesy, and hydrology, paper presented at *Proc.: 42nd Workshop on Geothermal Reservoir Engineering*, Stanford University, Stanford, California, 13–15 February 2017.

Feigl, K. L., and PoroTomo Team (2018). Overview and preliminary results from the PoroTomo project at Brady Hot Springs, Nevada: Poroelastic tomography by adjoint inverse modeling of data from seismology, geodesy, and hydrology, *Proc.: 43rd Workshop on Geothermal Reservoir Engineering*, Stanford University, Stanford, California, 12–14 February 2018.

Ikuta, R., K. Yamaoka, K. Miyakawa, T. Kunitomo, and M. Kumazawa (2002). Continuous monitoring of propagation velocity of seismic wave using ACROSS, *Geophys. Res. Lett.* **29,** 1627–1630.

Jolie, E. (2014). Detection and characterization of permeable fault zones by surface methods in the Basin-and-Range Province, USA, *Ph.D. Thesis*, Technische Universität, Berlin, 132 pp.

Jolie, E., I. Moeck, and J. E. Faulds (2015). Quantitative structural-geological exploration of fault-controlled geothermal systems—A case study from the Basin-and-Range Province, Nevada (USA), *Geothermics* **54,** 54–67.

Lancelle, C. (2016). Distributed acoustic sensing for imaging near-surface geology and monitoring traffic at Garner Valley, California, *Ph.D. Thesis*, University of Wisconsin-Madison, 108 pp.

Li, Z., Q. You, S. Ni, T. Hao, H. Wang, and C. Zhuang (2013). Waveform retrieval and phase identification for seismic data from the CASS experiment, *Pure Appl. Geophys.* **170,** 815–830.

Mateeva, A., J. Lopez, H. Potters, J. Mestayer, B. Cox, D. Kiyashchenko, P. Wills, S. Grandi, K. Hornman, B. Kuvshinov, W. Berlang, Z. Yang, and R. Detomo (2014). Distributed acoustic sensing for reservoir monitoring with vertical seismic profiling, *Geophys. Prospect.* **62,** 679–692, doi: 10.1111/1365-2478.12116.

Mavko, G., T. Mukerji, and J. Dvorkin (2009). *The Rock Physics Handbook: Tools for Seismic Analysis of Porous Media*, Cambridge University Press, Cambridge, United Kingdom, doi: 10.1017/CBO9780511626753.

Mestayer, J., B. Cox, P. Wills, D. Kiyashchenko, J. Lopez, M. Costello, S. Bourne, G. Ugueto, R. Lupton, G. Solano, D. Hill, and A. Lewis (2011). Field trials of distributed acoustic sensing for geophysical monitoring, *SEG Technical Program Expanded Abstracts 2011*, 4253-4257, Society of Exploration Geophysicists, Tulsa, Oklahoma.

Patterson, J., M. Cardiff, T. Coleman, H. Wang, K. Feigl, J. Akerley, and P. Spielman (2017). Geothermal reservoir characterization using distributed temperature sensing at Brady Geothermal Field, Nevada, *Leading Edge* **36,** no. 12, 1024a1–1024a7, doi: 10.1190/tle36121024a1.1.

Queen, J. H., T. M. Daley, E. L. Majer, K. T. Nihei, D. L. Siler, and J. E. Faulds (2016). Surface reflection seismic and vertical seismic profile at Brady's Hot Springs, NV, USA, *Proc.: 41st Workshop on Geothermal Reservoir Engineering*, Stanford University, Stanford, California, 22–24 February 2016, SGP-TR-209, 15 pp.

Saiga, A., K. Yamaoka, T. Kunitomo, and T. Watanabe (2006). Continuous observation of seismic wave velocity and apparent velocity using a precise seismic array and ACROSS seismic source, *Earth Planets Space* **58,** 993–1005.

Siler, D. L., N. H. Hinz, J. E. Faulds, and J. Queen (2016). 3D analysis of geothermal fluid flow favorability: Brady's, Nevada, USA, paper presented at *Proc. 41st Workshop on Geothermal Reservoir Engineering*, Stanford University, Stanford, California, 22–24 February 2016, SGP-TR-209, 10, https://pangea.stanford.edu/ERE/db/GeoConf/papers/SGW/2016/Siler.pdf (last accessed July 2018).

Sleeman, R., and T. van Eck (1999). Robust automatic P-phase picking: An on-line implementation in the analysis of broadband seismogram recordings, *Phys. Earth Planet. Int.* **113,** 265–275, doi: 10.1016/S0031-9201(99)00007-2.

Stokoe, K. H., E. M. Rathje, C. R. Wilson, B. L. Rosenblad, and F.-Y. Menq (2004). Development of the NEES large-scale mobile shakers and associated instrumentation for in situ evaluation of nonlinear characteristics and liquefaction resistance of soils, *13th World Conference on Earthquake Engineering*, Vancouver, British Columbia, 1–6 August 2004, http://www.iitk.ac.in/nicee/wcee/article/13_535.pdf (last accessed June 2017).

Thurber, C., and D. Eberhart-Phillips (1999). Local earthquake tomography with flexible gridding, *Comput. Geosci.* **25,** 809–818.

Trnkoczy, A. (2009). Understanding and parameter setting of STA/LTA trigger algorithm, in *New Manual of Seismological Observatory Practice*, Deutsches GeoForschungsZentrum GFZ, Potsdam, Germany, 965–984.

Um, J., and C. Thurber (1987). A fast algorithm for two-point seismic ray tracing, *Bull. Seismol. Soc. Am.* **77,** no. 3, 972–986.

Wang, H. F., X. Zeng, D. E. Miller, D. Fratta, K. L. Feigl, and C. H. Thurber (2018). Ground motion response to an M_L 4.3 earthquake using co-located distributed acoustic sensing and seismometer arrays, *Geophys. J. Int.* 213**,** 2020–2036, doi: 10.1093/gji/ggy102.

Wohletz, K., and G. Heiken (1992). *Volcanology and Geothermal Energy*, University of California Press, Berkeley, California, http://ark.cdlib.org/ark:/13030/ft6v19p151/ (last accessed July 2018).

Zeng, X., C. Lancelle, C. Thurber, D. Fratta, H. Wang, N. Lord, A. Chalari, and A. Clarke (2017). Properties of noise cross-correlation functions obtained from a distributed acoustic sensing array at Garner Valley, California, *Bull. Seismol. Soc. Am.* **107,** doi: 10.1785/0120160168.

L. M. Parker
C. H. Thurber
P. Li
N. E. Lord
H. F. Wang
A. Nayak
K. L. Feigl
Department of Geoscience
University of Wisconsin-Madison
Madison, Wisconsin 53706 U.S.A.
cthurber@wisc.edu

X. Zeng
State Key Laboratory of Geodesy and Earth's Dynamics
Institute of Geodesy and Geophysics
Chinese Academy of Sciences
Wuhan 430077, China

D. Fratta
Geological Engineering
Department of Civil and Environmental Engineering
University of Wisconsin-Madison
Madison, Wisconsin 53706 U.S.A.

M. C. Robertson
Earth & Environmental Sciences
Lawrence Berkeley National Laboratory
Berkeley, California 94720 U.S.A.

A. M. Thomas
Department of Earth Sciences
University of Oregon
Eugene, Oregon 97403 U.S.A.

M. S. Karplus
Department of Geological Sciences
The University of Texas at El Paso
El Paso, Texas 79902 U.S.A.